Journal of Solid State Chemistry 184 (2011) 2498–2505

Contents lists available at ScienceDirect

Journal of Solid State Chemistry

journal homepage: www.elsevier.com/locate/jssc

Structural and physical properties of the new intermetallic compound $Yb_3Pd_2Sn_2$

P. Solokha [a], I. Čurlik [b], M. Giovannini [a,*], N.R. Lee-Hone [c], M. Reiffers [b,d], D.H. Ryan [c], A. Saccone [a]

[a] Dipartimento di Chimica e Chimica Industriale, Università di Genova, Via Dodecaneso 31, 16146 Genova, Italy
[b] Institute of Experimental Physics, Watsonova 47, SK 043 53 Košice, Slovakia
[c] Physics Department and Centre for the Physics of Materials, McGill University, Montreal, Canada H3A 2T8
[d] Faculty of Sciences, University of Prešov, 17. Novembra 1, SK 080 78 Prešov, Slovakia

ARTICLE INFO

Article history:
Received 16 June 2011
Received in revised form
14 July 2011
Accepted 18 July 2011
Available online 23 July 2011

Keywords:
Ab initio powder structure determination
Stannides
Magnetic properties

ABSTRACT

The crystal structure of the ternary intermetallic compound $Yb_3Pd_2Sn_2$ has been determined *ab initio* from powder X-ray diffraction data. The compound crystallizes as a new structure type in the orthorhombic space group *Pbcm* and lattice constants $a=0.58262(3)$, $b=1.68393(8)$, $c=1.38735(7)$ nm. $Yb_3Pd_2Sn_2$ is composed of a complex $_\infty[Pd_2Sn_2]^{\delta-}$ polyanionic network in which the Yb ions are embedded. A comparison between this structure and those of $Eu_3Pd_2Sn_2$ and $Ca_3Pd_2Sn_2$, other novel polar intermetallic compounds, was made. DC susceptibility and ^{170}Yb Mössbauer spectroscopic measurements indicate a close-to divalent Yb behavior. Moreover, a hybridization between 4*f* and conduction electrons is suggested by electronic structure calculations and heat capacity measurements.

1. Introduction

Ytterbium and europium compounds show a great variety of anomalous physical phenomena, due to the fact that these lanthanides can exist in the trivalent or in the divalent state. In some compounds with two or more inequivalent crystallographic *R*-sites (*R*=rare earth metal), called heterogeneous mixed-valence systems, the divalent and trivalent oxidation states may coexist. These two states are $Yb^{3+}(4f^{13})$ / $Yb^{2+}(4f^{14})$ in case of Yb compounds and $Eu^{3+}(4f^{6})$ / $Eu^{2+}(4f^{7})$ for Eu intermetallics. A different situation is that of intermediate valence systems, where each lanthanide-ion has the same, non-integer valence due to hybridization of the 4*f* electrons [1].

A recent study on the isothermal section at 600 °C of the Yb–Pd–Sn system was published [2] motivated by the interesting physical properties of some of the ternary compounds in the system. One of the most interesting example is α- and β-YbPdSn. In fact, in α-YbPdSn only about 10% of the Yb^{3+} magnetic moments undergo magnetic ordering, while 90% are in a valence-fluctuating state [3]. Other intriguing examples are $YbPd_2Sn$ and Yb_2Pd_2Sn. $YbPd_2Sn$ is a peculiar Heusler compound, as it is one of the few examples of a Yb compound where superconductivity and magnetism coexist [4]. Yb_2Pd_2Sn crystallizes into the Mo_2FeB_2 type. For this compound, magnetic order appears and then vanishes by applying values of increasing pressure, indicating a possible occurrence of two quantum critical points [5]. A similar behavior was obtained by doping Sn sites by In [6]. In fact, the two compounds Yb_2Pd_2Sn and Yb_2Pd_2In [7] are isotypic and by In/Sn doping a continuous solution can be formed in the whole range of compositions.

In the investigation of the Yb–Pd–Sn system the formation of a new ternary compound with a tentative formula $Yb_3Pd_2Sn_2$ was reported [2]. Here we present the crystal structure and the physical properties of this compound. The crystal structure of $Yb_3Pd_2Sn_2$ was solved *ab initio* and it is compared with those of $Eu_3Pd_2Sn_2$ and $Ca_3Pd_2Sn_2$, novel ternary compounds, which were discovered in this work during the search of other analogous 3:2:2 compounds.

2. Experimental details and computational methods

2.1. Synthesis and characterization

The metals used were ytterbium (pieces, 99.993% Yb/TREM purity, Smart Elements GmbH, Vienna, Austria), palladium (foil, 99.95 mass% purity, Chimet, Arezzo, Italy), tin (bar, 99.999 mass% purity), europium and calcium (99.99 mass% purity, Smart Elements GmbH, Vienna, Austria). The samples, each with a total weight of 0.8–1 g, were prepared by weighing stoichiometric amounts of the elements. The elements were enclosed in small tantalum crucibles sealed by arc welding under pure argon, in

* Corresponding author.
E-mail address: giovam@chimica.unige.it (M. Giovannini).

0022-4596/$ - see front matter © 2011 Elsevier Inc. All rights reserved.
doi:10.1016/j.jssc.2011.07.031

order to avoid the losses of Yb and Eu due to their high vapor pressures. The samples were melted in an induction furnace, under a stream of pure argon. The samples were then generally annealed in a resistance furnace at 600 °C for three weeks and finally quenched in cold water. After quenching, samples were characterized by scanning electron microscopy (SEM) supplied by Carl Zeiss SMT Ltd., Cambridge, England, and electron probe micro-analysis (EPMA) based on energy dispersive X-ray spectroscopy. For quantitative analysis an acceleration voltage of 20 kV was applied for 100 s, and a cobalt standard was used for calibration. The X-ray intensities were corrected for ZAF effects. Attempts to grow single crystals of $Yb_3Pd_2Sn_2$ have been made using different thermal cycles, but all the trials were unsuccessful.

2.2. Data acquisition, structure analysis and refinement

The crystal structure of $Yb_3Pd_2Sn_2$ has been determined *ab initio* from X-ray powder diffraction data. The XRD data were collected at room temperature on a X'Pert MPD diffractometer (Philips, Almelo, The Netherlands) equipped with a graphite monochromator installed in the diffracted beam (Bragg Brentano, Cu$K\alpha$ radiation, for other details see Table 1). In the powder pattern of $Yb_{42}Pd_{29}Sn_{29}$ sample distinct peaks indexing was performed with the programs DICVOL06 [8] and N-TREOR implemented into EXPO [9], and the best figure of merit (FOM) was obtained for an orthorhombic cell with $a=1.68369$, $b=1.38757$, $c=0.58272$ nm. Profile parameters were derived from the Le Bail fit (FULLPROF program [10]). The analysis of the Bragg reflection conditions led to the possible extinction symbols *Pn–a*, *Pb–a* and *Pc–a* with similar FOM values, corresponding to the possible space groups $Pn2_1a$, *Pnma*, $Pb2_1a$, *Pbma*, *Pc2a* and *Pcma*. The mass density and the average volume per atom ($\sim$0.023 nm^3) of the compound were estimated from the known density and averaged atomic volumes of other ternaries in the Yb–Pd–Sn system. From these data, combined with the measured composition of the phase, the number of atoms in the unit cell could be estimated to be 54–60. The structure solution was found in the direct space by global optimization of the parameters using the program FOX [11]. During the global optimization, antibump distance restraints were used. Moreover, the presence of small impurity phases was taken into account in the procedure. Starting from the highest symmetries, the structure solution in the space group *Pnma* (62) was not successful. The second tested *Pbma* (57) group gave a very promising model with 56 atoms in unit cell (24 Yb, 16 Pd and 16 Sn atoms). This trial model was tested and refined with the Rietveld method using FULLPROF [10]. To check the proper composition, the occupancy parameters were varied in a separate series of least-squares cycles for each kind of atom. The occupancies did not vary noticeably and were always close to 100%, therefore they were fixed to be unity. Low and even negative values of refined displacement parameters were obtained. These values could be associated with the phenomenon of micro-absorption caused by the high linear absorption coefficient of the studied compound at the wavelength of the Cu$K\alpha$ radiation. The values were fixed in further cycles of refinement. As *Pbma* is a non-conventional setting of space group, the structural model was transformed into the standard space group *Pbcm*. Refined positional parameters have been standardized by *STRUCTURE TIDY*

Table 1
Crystallographic data, details of the structure refinement and standardized atomic coordinates of the $Yb_3Pd_2Sn_2$ structure.

Compound				**$Yb_3Pd_2Sn_2$**		
Sample composition (at%)				$Yb_{42}Pd_{29}Sn_{29}$		
Phase composition (at%)				$Yb_{42}Pd_{29}Sn_{29}$		
Abundance (wt%)				86.6		
Diffractometer; radiation				X'Pert MPD, Cu$K\alpha$		
2θ range (deg.); number of points				20÷100; 4001		
Step size (deg.); counting time (s)				0.02; 38		
Number of "independent" and "effective" reflections				939 761		
Number of refined structural parameters				21		
Crystal system				Orthorhombic		
Space group (No.)				*Pbcm* (57)		
Structure type				$Yb_3Pd_2Sn_2$		
Pearson symbol, Z				*oP*56, 8		
Unit-cell parameters:						
a (nm)				0.58262(3)		
b (nm)				1.68393(8)		
c (nm)				1.38735(7)		
Cell volume V (nm^3)				1.3611(1)		
Reliability factors:						
R_F (%)				6.35		
R_B (%)				8.47		
R_P (%)				8.9		
R_{wp} (%)				15.2		
Atom	**Wyckoff position**	***x*/*a***	***y*/*b***	***z*/*c***	**CN**	**VDP volume (Å^3)**
Pd1	8*e*	0.019(2)	0.3517(5)	0.0903(10)	11	21.02
Yb1	8*e*	0.196(1)	0.6778(4)	0.0981(7)	17	27.13
Pd2	8*e*	0.281(2)	0.1146(6)	0.0889(9)	10	20.21
Yb2	8*e*	0.505(2)	0.4296(4)	0.0973(6)	17	27.60
Yb3	4*d*	0.004(3)	0.5108(6)	1/4	17	28.27
Yb4	4*d*	0.295(2)	0.2437(7)	1/4	17	28.09
Sn1	4*d*	0.503(3)	0.0650(8)	1/4	12	22.93
Sn2	4*d*	0.209(2)	0.8275(8)	1/4	12	23.63
Sn3	4*c*	0.308(2)	1/4	0	16	22.05
Sn4	4*a*	0	0	0	14	23.38

Displacement parameters for $Yb_3Pd_2Sn_2$ were fixed: $B_{Yb}=0.9$, $B_{Sn}=1.1$, $B_{Pd}=1.3$ (nm$^2\times10^2$).

Table 2
Atomic coordinates of the $Eu_3Pd_2Sn_2$ structure. Space group *Pbcm*, $Z=4$, $La_3Ni_2Ge_2$ structure type; $a=0.60335(2)$ $b=0.87554(4)$ $c=1.41087(7)$ nm.

Atom	Wyckoff position	*x*/*a*	*y*/*b*	*z*/*c*	CN	VDP volume (Å^3)
Eu1	8*e*	0.147(1)	0.108(1)	0.0979(4)	17	30.59
Eu2	4*d*	0.643(2)	0.251(1)	1/4	17	30.85
Sn1	4*c*	0.638(2)	1/4	0	14	24.48
Sn2	4*d*	0.154(2)	0.397(1)	1/4	11	25.62
Pd1	8*e*	0.383(1)	0.4678(7)	0.0877(4)	10	22.10

program [12] (see Table 1). The refined lattice parameters in the standardized space group are $a=0.58262(3)$, $b=1.68393(8)$, $c=1.38735(7)$ nm.

As mentioned above, together with the new phase the sample contains two additional phases: 4.8 wt% of hexagonal YbPdSn (structure type ZrNiAl, space group $P\bar{6}2m$) and 8.5 wt% of orthorhombic YbPdSn (structure type TiNiSi, space group *Pnma*) [13]. Because of their small amounts and slight contribution to the diffraction pattern, these phases were refined with scale factors and 5 cell parameters, while the profile parameters were constrained to those of the main $Yb_3Pd_2Sn_2$ phase. In the final refinement cycles for $Yb_3Pd_2Sn_2$ 44 parameters were allowed to vary: zero shift, 3 scale factors, 3 cell parameters, 6 profile parameters (Pseudo-Voigt peak shape function with asymmetry), 21 positional parameters. Moreover, 63 background points were selected in the measured 2θ range.

A few late trivalent rare earths were selected with the purpose to synthesize isostructural compounds, but no other $R_3Pd_2Sn_2$ isotypic phase was found to exist. Instead, Eu gave promising results showing the presence of $Eu_3Pd_2Sn_2$ as main phase (SEM/EMPA results show also the presence of small amounts of EuPdSn [14] compound). Nevertheless, collected XRD of $Eu_3Pd_2Sn_2$ did not match with the structural model of $Yb_3Pd_2Sn_2$. An indexation of this dataset was performed giving an orthorhombic unit cell with $a=0.6033$, $b=0.8755$, $c=1.4109$ nm. These values are close to those of the prototype $La_3Ni_2Ge_2$ [15]. In fact, starting from this model, XRD data of $Eu_3Pd_2Sn_2$ were successfully refined with the Rietveld method using FULLPROF [10] (see Table 2). Finally, a sample of nominal composition $Ca_3Pd_2Sn_2$ was synthesized to verify the 3:2:2 phase formation. Beside the dominant $Ca_3Pd_2Sn_2$ phase, the sample contained CaPdSn and some unknown ternary phases. The XRD pattern of $Ca_3Pd_2Sn_2$ matched well with the above mentioned $Yb_3Pd_2Sn_2$ structural model. Due to the presence of unknown phases, the atomic coordinates have not been refined. The refined lattice parameters of $Ca_3Pd_2Sn_2$ are $a=0.5879(2)$, $b=1.6915(3)$, $c=1.3962(3)$ nm.

2.3. Measurements of heat capacity, electrical resistivity and magnetism

Heat capacity and electrical resistivity measurements were performed by a Physical Property Measurement System (PPMS) commercial device (Quantum Design) in the temperature range 0.4–300 K and in applied magnetic field up to 9 T. Heat capacity was measured using the two-τ model of the relaxation method. Electrical resistivity was carried out using a standard four-probe technique. Susceptibility was measured by a Magnetic Property Measurements System (MPMS) commercial device (Quantum Design) in the temperature range 2–300 K and in an applied field up to 5 T.

2.4. ^{170}Yb Mössbauer spectroscopy measurements

Finely powdered $Yb_3Pd_2Sn_2$ was loaded into a sample holder with Kapton windows. Transmission mode ^{170}Yb Mössbauer spectra were obtained with both the source and sample located in a helium flow cryostat at a common temperature. The available sample mass of 930 mg was somewhat below optimum but gave an absorption of about 1% at 5 K. The 20 mCi ^{170}Tm source was prepared by neutron activation of ~25 mg of Tm as a 10 wt% alloy in aluminum. A high-purity Ge detector was used to isolate the 84.26 keV γ-photons used for ^{170}Yb Mössbauer spectroscopy from the various other X-rays emitted by the source. Calibration of the spectrometer was achieved using a laser interferometer mounted on the back of the drive. Velocities were cross-checked against both ^{57}Co/α-Fe at room temperature and the ^{155}Gd Mössbauer spectrum of $GdFe_2$ at 5 K. Temperature stability was better than 0.01 K. The ^{170}Yb spectra were fitted using non-linear least-squares minimization routine to a sum of Lorentzian lines with positions and intensities obtained from diagonalization of the full nuclear hyperfine Hamiltonian [16].

2.5. Electronic structure calculation

Electronic structure calculations on $Yb_3Pd_2Sn_2$ were performed using the linear muffin-tin orbital (LMTO) method [17–19] in its tight-binding representation [20], which corresponds to a fast linearized form of the Korringa–Kohn–Rostoker (KKR) method [21,22]. The calculations using basis sets composed of short-ranged atom-centered TB-LMTOs without empty spheres were carried out using the TB-LMTO-ASA 4.7 program with a scalar-relativistic Hamiltonian and the atomic-spheres approximations [23]. Electronic energies were calculated via density–functional theory (DFT) based on the local-density approximation (LDA) for the exchange-correlation functional as parametrized by von Barth and Hedin [24]. In case of $Yb_3Pd_2Sn_2$ the addition of empty spheres was not necessary. The following radii of atomic spheres were applied for calculations: r(Yb)=1.821–2.086 Å, r(Pd)=1.450; 1.473 Å, r(Sn)=1.627–1.890 Å. The atomic overlap did not exceed 10%.

3. Results and discussion

3.1. Magnetic measurements

The temperature dependence of the DC susceptibility for $Yb_3Pd_2Sn_2$ at 1000 Oe is presented in Fig. 1. A very weak temperature dependence in the whole temperature range with a small upturn at low temperatures is shown. The nearly constant susceptibility indicates a close to divalent-Yb behavior. The value

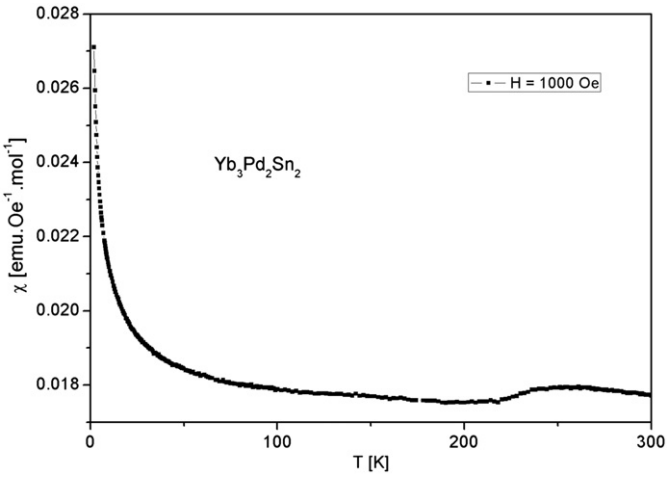

Fig. 1. Temperature dependence of DC magnetic susceptibility of $Yb_3Pd_2Sn_2$ at $H=1000$ Oe.

of the Pauli susceptibility $\chi(0)$, extrapolated to 0 K, is 0.018 emu/mol Oe. However, a tiny broad bump above 200 K may indicate that a minor part of the 4*f* level is unoccupied and, thus, some degree of *c*–*f* hybridization may arise. The small increase of susceptibility at lower temperatures is expected to be due to paramagnetic impurities.

In case of $Eu_3Pd_2Sn_2$ inverse susceptibility trend in the paramagnetic regime follows the Curie–Weiss law, yielding an effective magnetic moment of $\mu_{eff}=7.94\ \mu_B$, which is in exact agreement with the theoretical value for Eu^{2+}. The paramagnetic Curie temperature $\theta_P=-5$ K is negative indicating the presence of antiferromagnetic exchange.

3.2. Electrical resistivity

In Fig. 2 the normalized temperature dependence of electrical resistivity $\rho(T, B)$ of $Yb_3Pd_2Sn_2$ is shown as the function of an applied magnetic field up to 9 T. The resistivity decreases with decrease in temperature as is typical for ordinary metals. No pronounced anomalies were detected down to 0.4 K. Residual resitivity ratio RRR=7.5 at $B=0$ T confirms good quality of the polycrystalline sample. By increasing the magnetic field the RRR values decrease. Moreover, the residual resistivity ρ_0 values are also increasing, which is due to the Lorentz force.

3.3. Heat capacity

The measurement of temperature dependence of heat capacity for $Yb_3Pd_2Sn_2$ shows simple behavior without tendency to magnetic ordering up to 0.4 K. In Fig. 3 low temperature detail of *C*(T) in the temperature range 0.4–20 K and in applied magnetic field up to 9 T is shown. Heat capacity was not influenced by applied magnetic field up to 9 T, which implies a negligible magnetic contribution to heat capacity. This behavior is characteristic of ordinary metal with no sign of phase transition. However, fitting the *C*(T)/*T* versus T^2 dependence at low temperature and extrapolating to $T=0$ K yields an electronic Sommerfeld coefficient γ of 67 mJ mol^{-1} K^{-2}. The value of the electronic component, enhanced compared to ordinary metals, suggests an hybridization between 4*f* and conduction electrons.

3.4. ^{170}Yb Mössbauer spectroscopy

The diamagnetic closed shell structure of divalent ytterbium (Yb^{2+}) eliminates local contributions to the electric field gradient at the nucleus so that only the much weaker effects due to the

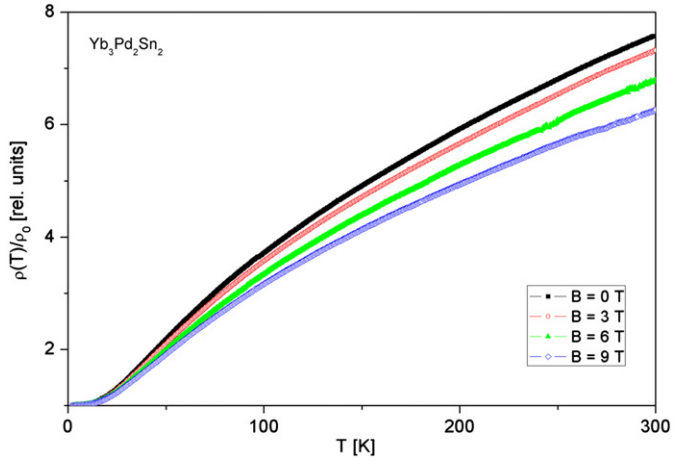

Fig. 2. Electrical resistivity as a function of temperature for $Yb_3Pd_2Sn_2$ for different magnetic fields up to 9 T; ρ_0=residual resistivity.

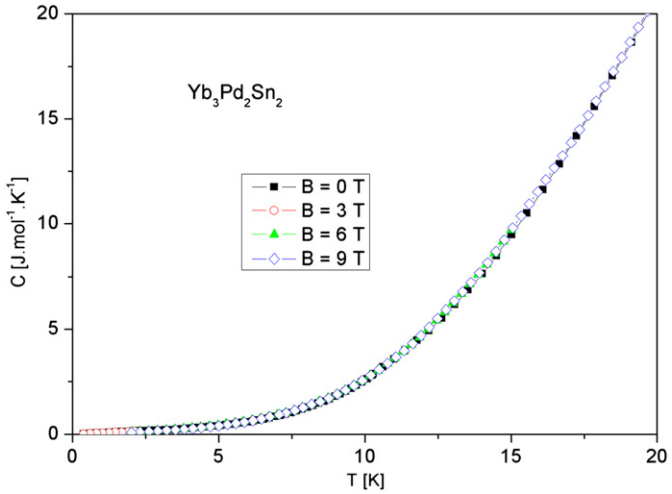

Fig. 3. Heat capacity of $Yb_3Pd_2Sn_2$ for different magnetic fields (up to 9 T) in the temperature range 0.4–20 K.

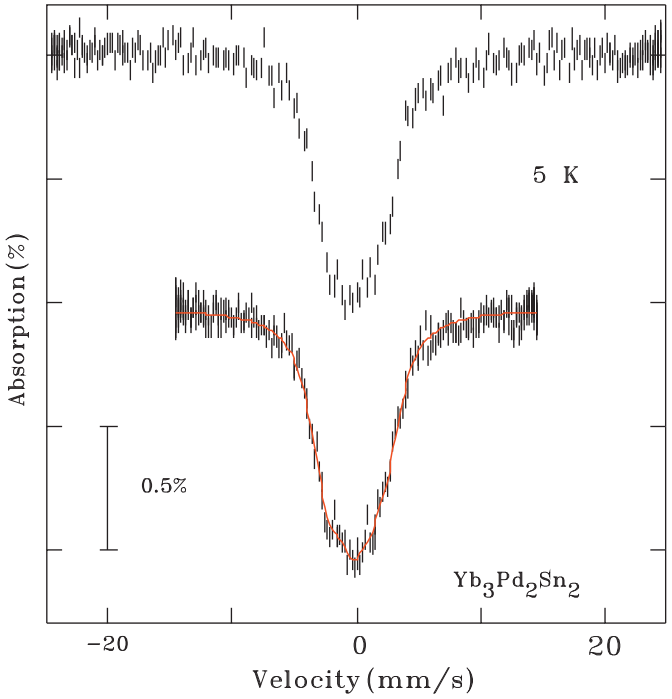

Fig. 4. ^{170}Yb Mössbauer spectrum of $Yb_3Pd_2Sn_2$ at 5 K. The solid line is a fit described in the text. The upper spectrum is from the same sample obtained on a wider velocity scale to confirm that there were no contributions from trivalent ytterbium present.

arrangement of the first neighbors are present. As a result, the Mössbauer spectra of divalent ytterbium compounds show small quadrupole effects (eQV_{zz}) of a few mm/s, compared some tens of mm/s seen for trivalent ytterbium compounds where a significant contribution from the last unpaired 4*f* electron is seen.

The 5 K ^{170}Yb Mössbauer spectrum of $Yb_3Pd_2Sn_2$ presented in Fig. 4 shows a somewhat broadened single feature centered on zero velocity, strongly suggesting the presence of only divalent ytterbium (Yb^{2+}). Measurements made on a wider velocity scale showed no evidence for additional components that could be attributed to either paramagnetic or magnetically ordered trivalent ytterbium (Yb^{3+}). The multiple crystallographic sites occupied by the ytterbium, coupled with the almost complete absence of resolved features, precludes a detailed fitting of the spectrum. However, a highly

constrained fit with four sites in the crystallographic ratio 2:2:1:1 and assuming only axially symmetric electric field gradients, yields a quite reasonable linewidth of 1.3(1) mm/s and an average magnitude for eQV_{zz} of $\langle|eQV_{zz}|\rangle \sim 8$ mm/s. There is no large mis-fit in the data that would suggest that either a weak (~17%) or stronger (~33%) site holding trivalent ytterbium had been missed.

Measurements taken up to 40 K (the rapid decline in the recoil-free fraction with increasing temperature makes it impossible to record ^{170}Yb Mössbauer spectra much above this temperature) showed no evidence for a change in the shape of the observed spectrum so we conclude that the ytterbium in $Yb_3Pd_2Sn_2$ remains divalent between 5 and 40 K.

3.5. Electronic structure of $Yb_3Pd_2Sn_2$

The total and projected densities of states for $Yb_3Pd_2Sn_2$ are shown in Fig. 5. The Fermi level (E_F) lies in a continuous density of states (DOS) region indicating a metallic character for the title compound, as confirmed by electrical resistivity measurements. Although a reliable localization of the 4*f* band in a LDA calculation is not trivial, the general DOS trend in the valence band (VB) exhibits similar features of other Yb-containing polar intermetallics [25,26]—a sharp distinct peak of Yb states close to the Fermi level that implies that, to a certain degree, hybridization exists between 4*f* and conduction electrons (*c*–*f* hybridization) for Yb ions. At the energies $E \leq -1$ eV the DOS shows mainly tin and palladium contributions to the VB.

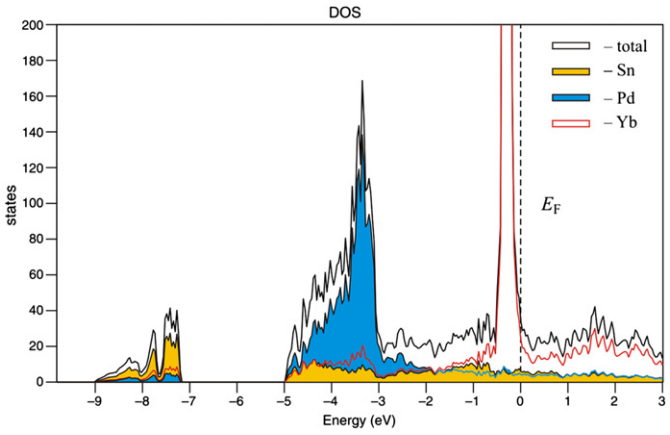

Fig. 5. Total and projected DOS for $Yb_3Pd_2Sn_2$.

The interatomic distances of $Yb_3Pd_2Sn_2$ are listed in Table 3. It is worth noting that the major part of Pd-Sn contacts are shorter that the sum of metallic radii of constituents (0.277 nm) [27]. These contact contractions support the strong tendency of Pd and Sn in forming chemical bonds evidenced by the inspection of the site projected DOS curves. In the following paragraph the structural features derived by the above-mentioned interactions will be described.

3.6. Phase formation and crystallochemical peculiarities of $Yb_3Pd_2Sn_2$ and $Eu_3Pd_2Sn_2$

The samples prepared on the atomic compositions 42 at% Yb, 29 at% Pd and 29 at% Sn and 42 at% Eu, 29 at% Pd and 29 at% Sn proved to be almost single phase. Nevertheless, a small amount of secondary phase with equiatomic composition 1:1:1 was detected by SEM and EPMA analyses. The analogous sample prepared on the composition 42 at% Ca, 29 at% Pd and 29 at% Sn present $Ca_3Pd_2Sn_2$ as dominant phase, and two secondary phases (CaPdSn and an unknown phase with composition 31 at%, 43 at% Pd, 26 at% Sn) were present in a significant amount.

The relevant crystallographic details for the data collection and refinement for $Yb_3Pd_2Sn_2$ and $Eu_3Pd_2Sn_2$ are listed in Tables 1 and 2, respectively. Observed, calculated and differential X-ray powder diffraction patterns of the $Yb_{42}Pd_{29}Sn_{29}$ sample are plotted in Fig. 6.

Table 3
Interatomic distances (< 0.35 nm) within the first coordination spheres for $Yb_3Pd_2Sn_2$. The contacts within $_\infty[Pd_2Sn_2]^{\delta-}$ network are shown in bold.

Central atom	Adjacent atoms	δ (nm)	Central atom	Adjacent atoms	δ (nm)	Central atom	Adjacent atoms	δ (nm)
Yb1	Pd1	0.2942	Yb4	2Pd2	0.3119	Sn4	**2Pd1**	**0.2796**
	Pd2	0.2980		Sn2	0.3216		**2Pd2**	**0.2816**
	Pd1	0.3188		Sn1	0.3244		2Yb2	0.3398
	Pd2	0.3229		Sn2	0.3258		2Yb2	0.3447
	Sn2	0.3287		2Pd1	0.3286		2Yb3	0.3473
	Sn1	0.3335		2Sn3	0.3471		2Yb1	0.3482
	Sn3	0.3417						
	Sn3	0.3458	Sn1	**2Pd2**	**0.2714**	Pd1	**Sn2**	**0.2616**
	Sn4	0.3482		Yb3	0.3014		**Sn3**	**0.2708**
				Yb3	0.3092		**Sn4**	**0.2796**
Yb2	Pd2	0.2988		2Yb2	0.3113		Yb1	0.2415
	Sn1	0.3113		Yb4	0.3244		Pd2	0.2972
	Pd1	0.3121		2Yb1	0.3335		Yb2	0.3121
	Sn2	0.3197					Yb1	0.3188
	Pd1	0.3273	Sn2	**2Pd1**	**0.2616**		Yb2	0.3273
	Pd2	0.3357		2Yb2	0.3197		Yb4	0.3286
	Sn4	0.3398		Yb4	0.3216		Yb3	0.3478
	Sn4	0.3447		Yb4	0.3258			
				2Yb1	0.3287	Pd2	**Sn3**	**0.2597**
Yb1	Sn1	0.3014		Yb3	0.3327		**Sn1**	**0.2714**
	Sn1	0.3092					**Sn4**	**0.2160**
	2Pd2	0.3288	Sn3	**2Pd2**	**0.2597**		Pd1	0.2972
	Sn2	0.3327		**2Pd1**	**0.2708**		Yb1	0.2980
	2Sn4	0.3473		2Yb1	0.3417		Yb2	0.2988
	2Pd1	0.3478		2Yb1	0.3458		Yb4	0.3119
				2Yb4	0.3471		Yb1	0.3229
				2Yb2	0.3505		Yb3	0.3288
							Yb2	0.3357

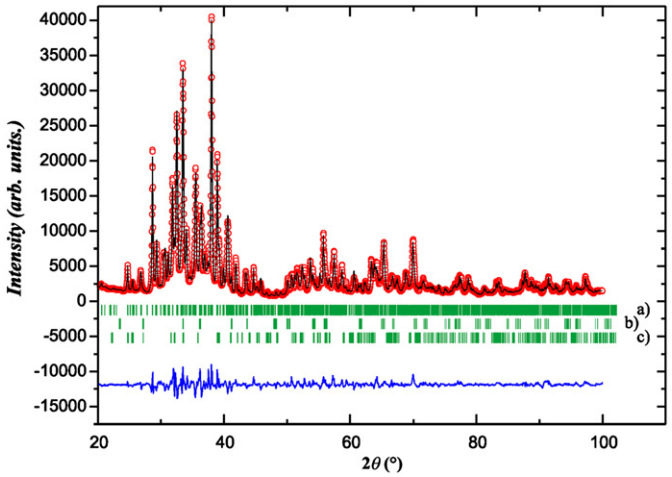

Fig. 6. Observed (circles), calculated (line) and difference (bottom line) X-ray powder diffraction patterns for $Yb_{42}Pd_{29}Sn_{29}$. Vertical bars indicate the Bragg positions of corresponding phases: (a) $Yb_3Pd_2Sn_2$, (b) YbPdSn (hexagonal) and (c) YbPdSn (orthorhombic).

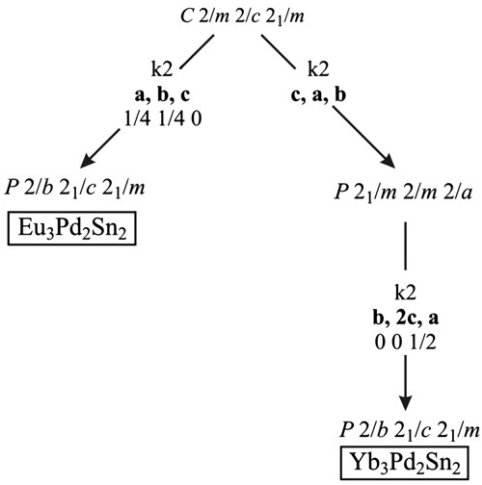

Fig. 8. Group–subgroup relation in the *Bärnighausen* formalism for the structures $Eu_3Pd_2Sn_2$ and $Yb_3Pd_2Sn_2$. The indices of the *klassengleiche* (k) transitions, the shifts in origin, and the unit cell transformations are given.

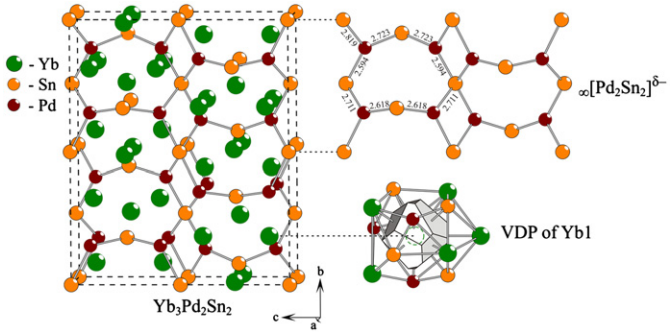

Fig. 7. Crystal structure of $Yb_3Pd_2Sn_2$ with outlined polyanionic networks of $_\infty[Pd_2Sn_2]^{\delta-}$ composition. In the top right corner the distances of heterogeneous Pd–Sn contacts within $_\infty[Pd_2Sn_2]^{\delta-}$ network are indicated. In the bottom the VDP together with closest neighbors for Yb1 are illustrated.

The most convenient relation between $Yb_3Pd_2Sn_2$ (or $Ca_3Pd_2Sn_2$) and $Eu_3Pd_2Sn_2$ structures can be shown comparing their polyanionic $_\infty[Pd_2Sn_2]^{\delta-}$ networks, which are characteristic for polar intermetallics. In the case of $Eu_3Pd_2Sn_2$ this polyanionic framework is quite regular with a smooth distribution of the heteroatomic Pd–Sn distances (see Fig. 1S). The substitution of bigger Eu atoms by Yb/Ca species results in the formation of a new related structure with a somewhat different $_\infty[Pd_2Sn_2]^{\delta-}$ network (see Fig. 7). In both cases polyanionic networks have pronounced 2D characters and, making an analogy with structural organic chemistry, could be defined as *cis*-$[Pd_2Sn_2]_\infty$ and *trans*-$[Pd_2Sn_2]_\infty$ conformations for $Eu_3Pd_2Sn_2$ and $Yb_3Pd_2Sn_2$ (or $Ca_3Pd_2Sn_2$), respectively.

The outlined changes in the crystal structures of $Eu_3Pd_2Sn_2$ and $Yb_3Pd_2Sn_2$ can be formalized by means of a group-subgroup relation [28] in the Bärnighausen-tree formalism (Fig. 8). The relations between the Wyckoff positions of the involved space groups were checked with the aid of the POWDER CELL program [29] and the Bilbao crystallographic server [30]. Both the crystal structures of $Eu_3Pd_2Sn_2$ and $Yb_3Pd_2Sn_2$ have *Cmcm* (No. 63) as common supergroup. Whereas $Eu_3Pd_2Sn_2$ adopts the *klassengleiche* subgroup of order 2 (*k*2) of the *Cmcm*-model, two steps are necessary to obtain the space group of the $Yb_3Pd_2Sn_2$ structure. The first step is a decentering through a *klassengleiche* reduction of index 2 (*k*2) giving the *Pmma*-model, followed by a doubling of one translation vector (in fact $b_{Yb3Pd2Sn2} \approx 2b_{Eu3Pd2Sn2}$) through a *klassengleiche* reduction (*k*2). These types of transformations are often lead to twin formation [31,32]. This may explain the difficulties in finding single crystals (see Section 2.2). It is worth mentioning that very similar group-subgroup relations to those discussed here were described for the analogous stannides $Eu_2Pt_3Sn_5$, $Yb_2Pt_3Sn_5$ and $Ca_2Pt_3Sn_5$ [30,33,34,35].

The structural peculiarities common to all these compounds can be described as $Yb_3Pd_2Sn_2$ composed of two blocks with the same composition—A and A′, stacked alternatively along the [0 1 0] direction. The blocks A′ are the mirror image of the blocks A (Fig. 9A). In a similar manner, the relations between $Eu_2Pt_3Sn_5$ and $Yb_2Pt_3Sn_5$ are shown in Fig. 9B. In the latter case, the blocks B are translated with respect to the analogous blocks B by 1/2, 1/2, 0.

In the crystal structure of $Yb_3Pd_2Sn_2$ the ytterbium atoms occupy four inequivalent crystallographic positions. Moreover, all these positions are characterized by similar coordination arrangements (see Table 3) and interatomic distances within the first coordination sphere are of comparable values. A possible scenario where $Yb_3Pd_2Sn_2$ is a heterogeneous mixed-valent compound is ruled out by the results of Mössbauer spectroscopy and susceptibility data. In order to search for a geometrical confirmation of the above-mentioned result, an analysis through the Voronoi–Dirichlet polyhedra (VDP) approach was performed using the TOPOS program package [36]. This analysis is very efficient in the case of identically coordinated atoms in comparable structures [37]. This is the case of $Yb_3Pd_2Sn_2$ and $Eu_3Pd_2Sn_2$, where structural differences do not provoke changes in closest arrangements of atoms and the volumes of VDP polyhedron of Yb in $Yb_3Pd_2Sn_2$ and Eu in $Eu_3Pd_2Sn_2$ are comparable (Tables 1 and 2). To give an estimate on the VDP volume changes for Yb^{3+},Yb^{2+}/Eu^{3+},Eu^{2+} atoms, data related to heterogeneous mixed-valent RE_3O_4 oxides are presented in Table 1S. From this table, the Eu^{2+} ion is about 1.12 times bigger than the Yb^{2+} ion. A very similar ratio (≈ 1.11) between Eu and Yb was obtained from the average values of VDP for Eu^{2+} in $Eu_3Pd_2Sn_2$ and Yb^{2+} in $Yb_3Pd_2Sn_2$ (measurements of susceptibility on $Eu_3Pd_2Sn_2$ indicated a Eu^{2+} oxidation state). Finally, the fact that $Ca_3Pd_2Sn_2$ is isotypic with $Yb_3Pd_2Sn_2$ (both atomic and ionic dimensions of Ca and Yb atoms are very close) is another strong indication that geometrical factors play a decisive role on the formation of structures in 3-2-2 compounds, and that the Yb atoms have a close to +2 oxidation state in $Yb_3Pd_2Sn_2$.

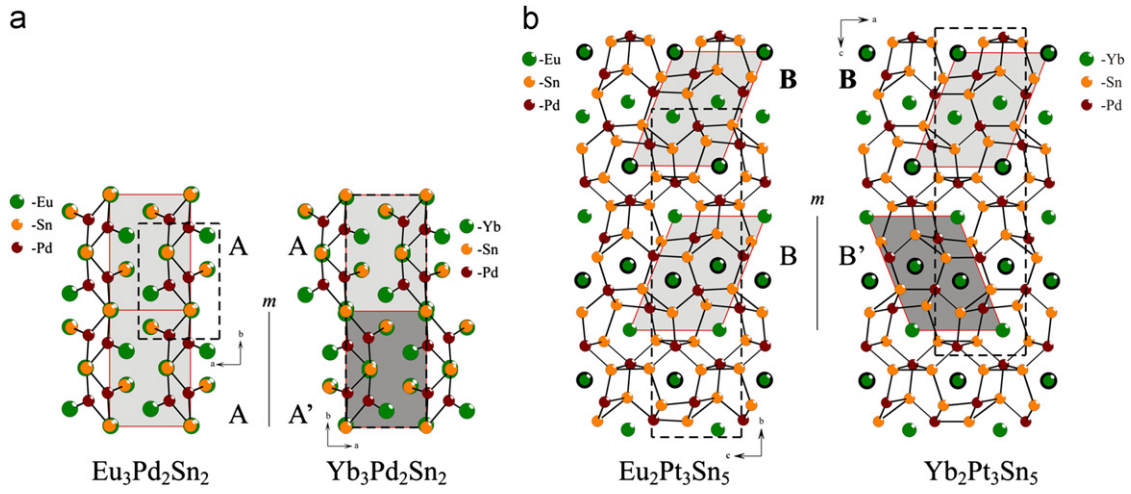

Fig. 9. Relationship between (a) $Eu_3Pd_2Sn_2$ and $Yb_3Pd_2Sn_2$ and (b) $Eu_2Pt_3Sn_5$ and $Yb_2Pt_3Sn_5$. Polyanionic networks $_\infty[Pd_2Sn_2]^{\delta-}$ and $_\infty[Pd_3Sn_5]^{\delta-}$ are outlined (unit cells are shown by dotted lines). Singled out fragments A and A′, B and B′ as mirror images of each other (for more details see text).

4. Conclusions

An *ab initio* determination of the crystal structure of the novel ternary compound $Yb_3Pd_2Sn_2$ has been performed. The Yb atoms were found to occupy four different crystallographic sites. Magnetic susceptibility, specific heat and resistivity measurements on $Yb_3Pd_2Sn_2$ show a close-to divalent Yb. Moreover, the results of electronic structure calculations, together with a value of the Sommerfeld coefficient higher than those of ordinary metals, point to a certain degree of hybridization of 4*f*- and conduction electrons. Nevertheless, a possible scenario where $Yb_3Pd_2Sn_2$ is a heterogeneous mixed-valent compound is ruled out by the results of ^{170}Yb-Mössbauer spectroscopy.

The crystal structure of 3:2:2 novel ternary compounds discovered in this work, $Eu_3Pd_2Sn_2$ and $Ca_3Pd_2Sn_2$, have been studied as well, and a comparison between the structures of the three compounds was made. According to the magnetic data in the paramagnetic regime, Eu result to be divalent. An investigation of the magnetism of $Eu_3Pd_2Sn_2$ at low temperatures, as well as on transport and heat capacity properties, is in progress.

Acknowledgments

This work has been partly supported by the Slovak-Italian Scientific-Technological Exchange Program for fellowships in Genova and Kosice; Slovak Research and Development Agency under the contract nos. APVV—SK-IT-0023-08 and VVCE-0058-07; the Slovak grant agency VEGA 2/0007/09; the CLTP as the Centre of Excellence of the Slovak Academy of Sciences and P.J. Šafárik University; the CEX Nanofluid as the Centre of Excellence SAS. The liquid nitrogen for the experiment in Kosice has been sponsored by the U.S. Steel Kosice, s.r.o. Financial support for various stages of this work was provided by the Natural Sciences and Engineering Research Council of Canada and Fonds Québécois de la Recherche sur la Nature et les Technologies. The ^{170}Yb source activation was carried out by M. Butler at the McMaster Nuclear Reactor (MNR), Hamilton Ontario.

Appendix A. Supporting information

Supplementary data associated with this article can be found in the online version at doi:10.1016/j.jssc.2011.07.031.

References

[1] P. Wachter, H. Boppart, (Eds.), in: Proceedings of the International Conference On Valence Instabilties, Zürich, Amsterdam, North-Holland, 1982.
[2] M. Giovannini, R. Pasero, A. Saccone, Intermetallics 18 (2010) 429–433.
[3] T. Görlach, S. Putselyk, A. Hamann, T. Tomanic, M. Uhlarz, F.M. Schappacher, R. Pöttgen, H.V. Löhneysen, Phys. Rev. B 76 (2007) 205112.
[4] B. Amato, P. Roessli, N. Fischer, A. Bernhoeft, C. Stunault, A. Baines, H.Sugawara Dönni, Physica B 326 (2003) 369–373.
[5] T. Muramatsu, T. Kanemasa, T. Kagayama, K. Shimizu, Y. Aoki, H. Sato, M. Giovannini, P. Bonville, V. Zlatic, I. Aviani, R. Khasanov, C. Rusu, A. Amato, K. Mydeen, M. Nicklas, H. Michor, E. Bauer, Phys. Rev. B 18 (2011) 180404(R).
[6] E. Bauer, G. Hilscher, H. Michor, C. Paul, Y. Aoki, H. sato, D.T. Adroja, J.G. Park, P. Bonville, C. Godart, J. Sereni, M. Giovannini, A. Saccone, J. Phys. Condens. Mater. 17 (2005) S999–S1009.
[7] M. Giovannini, E. Bauer, H. Michor, G. Hilscher, A. Galatanu, A. Saccone, P. Rogl, Intermetallics 9 (2001) 481–485.
[8] D.Louër Boultif, Indexing of powder diffraction patterns for low-symmetry lattices by the successive dichotomy method, J. Appl. Crystallogr. 24 (1991) 987–993.
[9] M. Altomare, C. Camalli, C. Cuocci, A. Giacovazzo, R.Rizzi Moliterni, *EXPO2009*: structure solution by powder data in direct and reciprocal space, J. Appl. Crystallogr. 42 (2009) 1197–1202.
[10] J. Rodriguez-Cavajal, Recent developments in the program FullProf, Newsletter 26 (2001) 12–19.
[11] V. Favre-Nicolin, R. Černý, FOX, "free objects for crystallography": a modular approach to ab initio structure determination from powder diffraction, J. Appl. Crystallogr. 35 (2002) 734–743.
[12] L. Gelato, E. Parthé, J. Appl. Crystallogr. 20 (1987) 139–143.
[13] D. Kuβman, R. Pöttgen, B. Künnen, G. Kotzyba, R. Müllmann, B.D. Mosel, Z. Kristallogr. 213 (1998) 356–363.
[14] R. Pöttgen, Z. Naturforsch. B 51 (1996) 806–810.
[15] K.A. Gschneidner, L. Eyring (Eds.), Handbook on the Physics and Chemistry of Rare Earths, volume 27, Elsevier, 1999.
[16] C.J. Voyer, D.H. Ryan, Hyp. Int. 170 (2006) 91.
[17] O.K. Andersen, Phys. Rev. B 12 (1975) 3060–3086.
[18] H. Skriver, The LMTO Method, Springer-Verlag, Berlin, 1984.
[19] O.K. Andersen, in: P. Phariseau, M. Temmerman (Eds.), In The Electronic Structure of Complex Systems, Plenum, New York, 1984.
[20] O.K. Andersen, O. Jepsen, Phys. Rev. Lett. 53 (1984) 2571–2574.
[21] J. Korringa, Physica 13 (1947) 392–400.
[22] W. Kohn, N. Rostoker, Phys. Rev. 94 (1954) 1111–1120.
[23] G. Krier, O. Jepsen, A. Burkhardt, O.K. Andersen, The TB-LMTO-ASA program, version 4.7; Max-Planck-Institut für Festkörperforschung, Stuttgart, Germany.
[24] U. von Barth, L. Hedin, J. Phys. C 5 (1972) 1629–1642.
[25] L. Vasylechko, W. Schnelle, M. Schmidt, U. Burkhardt, H. Borrmann a, U. Schwarz, Yu. Grin, J. Alloys Compd. 416 (2006) 35–42.
[26] A. Jezierski, D.Kaczorowski Szytuła, Mater. Sci.—Poland 24 (2006) 683–687.
[27] J. Emsley, Elements, Mir, Moscow, 1993 256 p. (in Russian, translated).
[28] H. Wondratshek, U. Müller (Eds.), Symmetry Relations Between Space Groups, vol. A1, Kluwer, Academic Publishers, Dordrecht, 2004.
[29] G. Nolze, POWDER CELL. Computer Program for the Calculation of X-ray Powder Diagrams, Bundesanstalt für Materialforschung, Berlin, 1996.
[30] E. Kroumova, M.I. Aroyo, J.M. Perez-Mato, S. Ivantchev, J.M. Igartua, H. Wondratschek, PSEUDO: a program for a pseudosymmetry search, J. Appl. Crystallogr. 34 (2001) 783–784.
[31] Ya. Galadzhun, R.-D. Hoffman, R. Pöttgen, M. Adam, J. Solid State Chem. 148 (1999) 425–432.

[32] U. Müller, Inorganic Structural Chemistry, Wiley, 2006.
[33] Y. Muro, K. Yamane, M.-S. Kim, T. Takabatake, C. Godart, P. Rogl, J. Phys. Soc. Jpn. 72 (2003) 1745–1750.
[34] T. Harmening, W. Hermes, M. Eul, F.M. Schappacher, R. Pöttgen, Z. Kristallogr. 224 (2009) 351–357.
[35] R.D. Hoffmann, D. Kuβmann, U.C. Rodewald, R. Pöttgen, C. Rosenhahn, B.D. Mosel, Z. Naturforsch. B 54 (1999) 709–717.
[36] V.A. Blatov, IUCr Comp. Comm. Newslett. 7 (2006) 4–38 〈http://www.topos.ssu.samara.ru〉.
[37] V. Blatov, Crystallogr. Rev. 10 (2004) 249–318.